Cobalt Complex of a Tetraamido Macrocyclic Ligand as a Precursor for Electrocatalytic Hydrogen Evolution

Xian Liang Ho,[a,b] Siva Prasad Das,[a,c] Leonard Kia-Sheun Ng,[a] Andrew Yun Ru Ng,[a,d] Rakesh Ganguly,[a] and Han Sen Soo*[a,b]

[a] Division of Chemistry and Biological Chemistry, School of Physical and Mathematical Sciences, Nanyang Technological University, Singapore 637371.

[b] Solar Fuels Laboratory, Nanyang Technological University, 50 Nanyang Avenue, Singapore 639798.

[c] Department of Chemistry, School of Science, RK University, Bhavnagar Highway, Kasturbadham, Rajkot – 360020, Gujarat, India.

[d] Institute of Materials Research and Engineering (IMRE), A*STAR (Agency for Science, Technology and Research), 2 Fusionopolis Way, Singapore 138634.

ABSTRACT: Hydrogen (H_2) is a clean fuel that can potentially store renewable energy and overcome some of the environmental problems that arise from fossil fuel consumption. One attractive approach is to produce H_2 from water electrocatalytically using molecular complexes that can be systematically improved through ligand modifications. Here, we report cobalt and nickel complexes supported by tetraamido macrocyclic ligands (TAML), which consist of exclusively earth abundant elements. Although TAML systems are well established in high valent transition metal chemistry, little is known about their reactivity in reductive catalysis despite the electron-rich nature of the tetraanionic TAML. Thus, we explored the utility of these nucleophilic -ate complexes as potential electrocatalysts for H_2 evolution using water as the proton source. Controlled potential electrolysis experiments were performed and the cobalt TAML variant exhibited catalytic H_2 evolution activity in acetonitrile containing 1.0 M water, but was inactive in purely aqueous solutions. Further investigation revealed that cobalt metal nanoparticles were electrodeposited as the active catalyst for H_2 evolution. We propose that these disparities in reactivity arise from the different number of water molecules coordinated to the cobalt center, with intermediate concentrations favoring a square pyramidal structure with labile ligands, whereas high concentrations of water result in a kinetically inert octahedral complex with no empty coordination sites.

INTRODUCTION

Electrocatalysis has experienced a renaissance lately with intense interest in their applications in materials,[1] energy,[2] and even synthetic organic chemistry.[3] Of special interest to us is the use of electrocatalysis as a fundamental component of artificial photosynthesis to address global climate change.[4] The consequences of increasingly palpable climate change have largely been recognized to originate from anthropogenic generation of greenhouse gases due to consumption of fossil fuels and the proliferation of volatile, halogenated organic compounds. A promising and more sustainable approach to overcome these problems is to harness solar or other renewable, but intermittent sources of energy to produce electricity, which can subsequently be employed in electrocatalytic processes to store energy in molecules such as hydrogen (H_2) and oxygen (O_2) by splitting water.[4-5]

Although water splitting electrocatalysis has traditionally been dominated by platinum group metals,[6] there has been increasing interest in the utilization of more earth-abundant, molecular, first-row transition metal systems,[4, 7] main group compounds,[8] and even recycled spent nuclear waste.[9] Molecular electrocatalysts for proton (H^+) reduction are especially attractive since they can be systematically customized by ligand modifications and some of them have demonstrated outstanding turnover frequencies (TOF) at modest overpotentials (η). For instance, inspired by natural hydrogenase enzymes, there have been reports of iron (Fe),[7c] nickel (Ni),[7e, 7f] and other late,[7c, 10] first-row transition metal electrocatalysts that operate in water. Among these reports, one of the themes that have proven successful at enhancing proton reduction catalytic activity has been the careful management of second coordination sphere effects to create H^+ relays and reduce the kinetic barrier for H_2 evolution.[7e, 7f, 11] Notably, however, not many of these catalysts are nucleophilic –ate complexes.

In an effort to develop the vital functions of artificial photosynthesis, our team has been working on creating molecular catalysts with exclusively earth-abundant elements.[4, 7f, 12] We designed Ni salicylaldimine electrocatalysts bearing chelating ether arms to direct Lewis acidic alkali metal cations and water molecules close to the Ni active site.[7f] These electrocatalysts could evolve H_2 in their reduced –ate forms from aqueous salt solutions, and even seawater.[7f] Moreover, we also examined the valence tautomerization in bona fide high-valent Fe tetraamido macrocyclic ligand (TAML) –ate complexes and observed an unusual nucleophilic addition and C-H activation on the TAML aromatic ring.[12f] The Fe TAML complexes had been pioneered by Collins and coworkers and have been utilized in many oxidative applications including pulp bleaching,[13]

decomposition of organic pollutants,[13d, 13g, 13h, 14] destruction of explosives,[15] and water oxidation.[16] Furthermore, Nam, Fukuzumi, and others have recently extended the applications of TAML compounds to other applications such as oxidative C-H activation by high-valent cobalt (Co) and Ni complexes.[13f, 17] These seminal studies highlight the oxidative robustness of TAML systems, but also underscore the paucity of reports on the reductive catalytic activity of these potentially nucleophilic late transition metal –ate complexes.

Herein, we explored the reactivity of Co and Ni TAML complexes under reductive conditions, specifically for electrocatalytic proton reduction. The TAML ligand is slightly modified compared to prior examples[17c, 17i, 17j] and all the metal complexes have been extensively characterized, including with X-ray structural studies. The Co TAML complex appeared to be active for electrocatalytic H_2 evolution in acetonitrile containing 1.0 M water, but detailed studies revealed that Co nanomaterials were responsible for the catalysis. By analyzing the electronic structure, we believe that coordination of different numbers of water molecules at the axial location alters the kinetic stability of the Co TAML complex, resulting in divergent reactivity at different concentrations of water.

RESULT AND DISCUSSION

SYNTHESIS AND NMR CHARACTERIZATION OF THE TAML COMPLEXES

The TAML compound was synthesized in a total of six steps (Scheme 1) from commercially available reagents. In the first step, 2,4-dibromo-2,4- dimethylpentanone (**1**) was subjected to S_N1 nucleophilic substitution conditions with sodium azide (NaN_3) to give 2,4-diazido-2,4- dimethylpentanone (**2**) under reflux conditions in ethanol. After extraction with pentane, the concentrated solution of **2** was used in the next step without further purification due to concerns over the safety of isolating large amounts of this potentially explosive, low molecular weight, organic aliphatic azide. Compound **2** was then reduced by lithium aluminium hydride to give 2,4-diamino-2,4-dimethylpentan-3-ol (**3**) in 79.6% yield. The third step of the ligand synthesis was the formation of the first amide linkage with α-bromoisobutyryl bromide in dichloromethane (DCM) to give bis-2,4-(2-bromo-2-methylpropanamido)-2,4-dimethyl-pentan-3-ol (**4**) with a yield of 88.1%. The reaction with

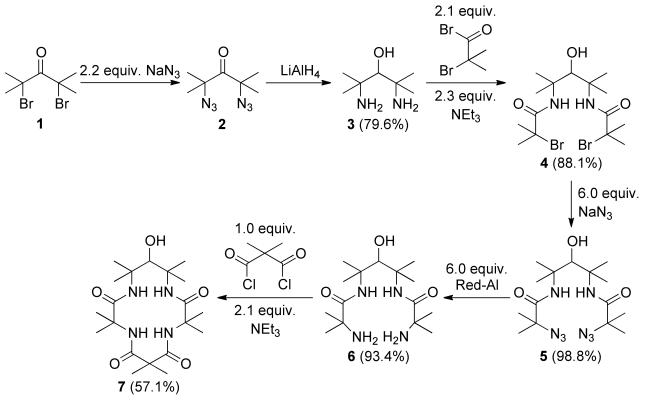

Scheme 1. Synthetic route to access the sterically encumbering TAML ligand **7.**

the acyl bromide is very exothermic and the reagent should be added slowly with care to avoid boiling the DCM. Compound **4** was then mixed with NaN_3 in another S_N1 nucleophilic substitution reaction to give bis-2,4-(2-azido-2-methylpropanamido)-2,4- dimethylpentan-3-ol (**5**) almost quantitatively. Likewise, **5** could be used without additional purification in the next step, where the azido groups were reduced using sodium bis(2-methoxyethoxy) aluminium hydride (Red-Al) in 70% toluene solution. Red-Al was found to be selective for reducing the azide without reacting with the amides and **6** was isolated in 93.4% yield. The final step for the ligand formation involved macrocycle ring closure with 2,2-dimethylmalonyl chloride *via* dropwise addition over 8 h under dilute conditions to prevent oligomerization. Compound **7** was isolated after purification by silica gel column chromatography as a colorless, crystalline material in 57.1% yield.

The metal complexes were synthesized by using a strong base, lithium bis(trimethylsilyl)amide (LiHMDS), to deprotonate **7** before the addition of different metal precursors to give their respective TAML metal complexes (Scheme 2). These complexes were fully characterized by nuclear magnetic resonance (NMR) spectroscopy, high- resolution mass spectrometry (HRMS), and elemental analyses.

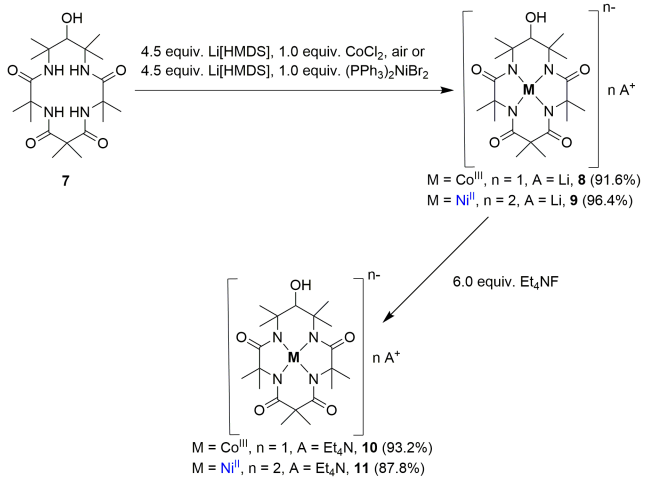

Scheme 2. Synthetic route to access the TAML complexes of Co^{III} and Ni^{II}.

Complex **9** is diamagnetic and displayed typical ^{1}H NMR features consistent with a square planar d^8 electronic configuration containing mirror symmetry. Remarkably, the ^{1}H NMR of **8** suggested the formation of a paramagnetic Co^{III} complex, instead of the common low-spin diamagnetic, octahedral Co^{III}.[17a] An Evan's method measurement was carried out to determine the magnetic susceptibility of the complex. Complex **8** is found to have an intermediate spin ground state with a spin-only magnetic moment of 2.91 μ_B, corresponding to a $S = 1$ ground state. In order to improve the solubility of complex **8** in organic solvent for further characterization, it was subjected to cation exchange with tetraethylammonium fluoride to give **10**. As anticipated, **10** became more soluble in a wider range of organic solvents, enabling the growth of single crystals for X-ray structural characterization.

STRUCTURAL CHARACTERIZATION BY SINGLE CRYSTAL X-RAY DIFFRACTION

Deep red plate-like single crystals of **10** were grown from DCM and diethyl ether, and a specimen was used for X-ray crystallography. The ORTEP of **10** is shown in Figure 1, and Table 1 summarizes the salient bond lengths and angles. Detailed information about the crystallographic experiment, including the remaining bond parameters, are given in the Supporting Information (SI).

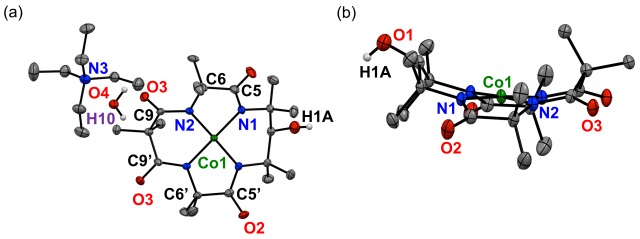

Figure 1. ORTEP of **10** with the thermal ellipsoids at 50% (a) with the tetraethylammonium cation and water included, and (b) showing the planar geometry around the Co center. The ellipsoids are colored according to their elements: Co (green), N (blue), O (red), C (gray), and H (white). A mirror plane bisects the Co centre. All hydrogen atoms have been omitted except for the ones on the water molecule and the alcohol group on the ligand.

Table 1. Selected bond distances and angles for 10.

Parameter	Bond length (Å)
Co1-N1	1.8720(19)
Co1-N2	1.8630(91)
C2-N1	1.485(3)
C5-N1	1.351(3)
C5-O2	1.239(3)
C6-N2	1.469(3)
C9-N2	1.361(3)
C9-O3	1.237(3)
C1-O1	1.400(4)
	Bond angle (°)
N1-Co1-N1	96.47(12)
N1-Co1-N2	84.59(8)
N2-Co1-N2	94.15(12)
N2-Co1-N1	176.38(9)
Co1-N1-C2	127.79(15)
Co1-N1-C5	114.07(16)
Co1-N2-C6	115.44(15)
Co1-N2-C9	125.60(16)

The Co center shows a square planar geometry with 4 N atoms at almost equal distances around the metal. The average distance between the Co and N atoms in **10** is 1.868 Å, which is close to the reported values for Co^{III} complexes.[18] The cis and trans N bond angles N1-Co1-N1 and N2-Co1-N1 are 96.47(12)° and 176.38(9)° respectively, illustrating how the Co is sitting almost exactly within the plane of the four N atoms (Figure 1b). The slight distortions from 90° and 180° of a perfect square planar complex likely arise from the steric constraints afforded by the macrocycle. In addition, the lone pair of electrons on the N are all delocalized to form some partial double bond character between N and the carbonyl carbon, resulting in shorter bond distances of 1.351(3) and 1.361(3) Å for C5-N1 and C9-N2, respectively. In contrast, the *bona fide* single bonds of C2-N1 and C6-N2 are 1.485(3) and 1.469(3) Å, respectively. Overall, these bond parameters concur with the (TAML)Co^{III} structural data reported by Collins and coworkers[19] and are consistent with the intermediate spin nature of the complex.

UV-VISIBLE SPECTROSCOPY OF TAML COMPLEXES

Complex **8** exhibits two intense absorption bands at 392 nm and 584 nm with molar extinction coefficients of 2020 and 3530 M^{-1} cm^{-1} respectively (Figure 2a), obtained from the Beer-Lambert Law, $A = \varepsilon Cl$ (A = absorbance; ε = molar extinction coefficient; C = concentration; l = pathlength of cell). The magnitude of these absorption bands suggest that they should arise ligand-to-metal charge transfer (LMCT), since the aliphatic **7** will be a poor π-acceptor. We propose that the LMCT originates from the electron-rich amide N to the $d_{xz/yz}$ and d_{z2} orbitals of the Co^{III} center in the square planar geometry.[17a]

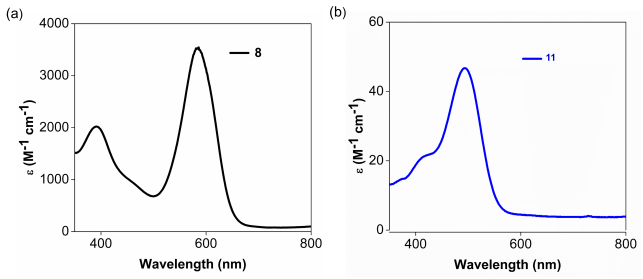

Figure 2. Plot of molar extinction coefficient against wavelength for (a) **8** (black), and (b) **11** (blue) in acetonitrile (ACN).

Complex **11**, however, exhibits only weak absorptions in the visible region with a peak at 492 nm, at an extinction coefficient of 47.1 M^{-1} cm^{-1} (Figure 2b). Complex **11** has a low-spin Ni^{II} d^8 electronic configuration with a high energy d_{x2-y2} orbital. Consequently, the LMCT transitions to the empty d_{x2-y2} orbital are likely to be much higher in energy. The weak absorption bands in the visible spectrum for **11** probably arise from d-d transitions instead.

CYCLIC VOLTAMMETRY OF TAML COMPLEXES

The cyclic voltammogram (CV) of **8** in ACN shows an quasi-reversible redox wave with an $E_{1/2}$ at -0.41V vs AgCl/Ag, which we assign to the Co^{III}/Co^{II} redox couple (Figure 3a).[20] On the other hand, **11** shows a reversible redox wave at +0.24 V (Figure 3b). This redox wave is assigned as the Ni^{III}/Ni^{II} redox couple.[21] We conducted CV experiments at different scan rates on each of these complexes as displayed in Figures 3c-d. The peak currents were then plotted against the square root of the scan rate according to

the Randles-Sevcik equation for both complexes **8** and **11** (Figures S1 and S2 respectively, SI). The redox wave for **8** is quasi-reversible, with the anodic wave at a higher current than the cathodic peak even up to 1000 mV s^{-1} (Figure S1, SI). On the other hand, the linear plots obtained from **11** confirm that the redox couple appear to be reversible at scan rates between 100 to 1000 mV s^{-1} (Figure S2, SI). The linear relation between the peak currents and the square root of the scan rates indicated that the redox processes for both **8** and **11** are under diffusion control. With these results in hand, we sought to explore if the electron-rich **8** and **11** could exhibit electrocatalytic reductive behavior.

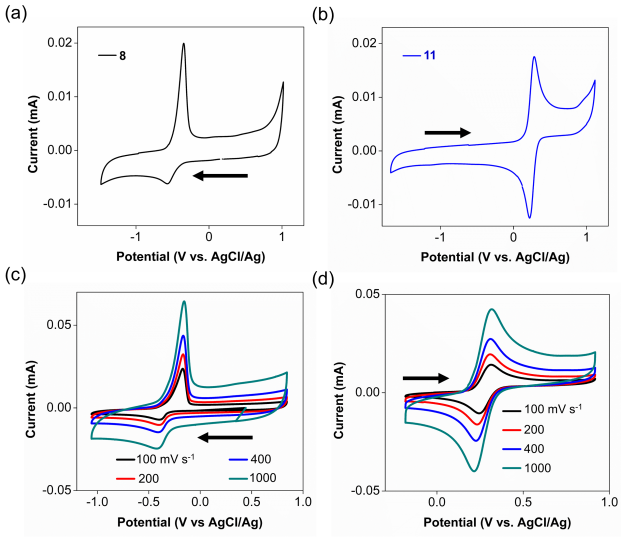

Figure 3. CVs of 1.0 mM (a) **8** (black) and (b) **11** (blue) in 0.10 M *n*-Bu_4NPF_6 solutions in ACN. Each experiment is conducted with a glassy carbon electrode (3 mm diameter) at a scan rate of 100 mV s^{-1}. Plot of CVs at scan rates of 100 (black), 200 (red), 400 (blue), and 1000 (teal) mV s^{-1} for complexes (c) **8** and (d) **11**. The black arrows correspond to the direction in which the initial potential was applied.

ELECTROCATALYTIC PROTON REDUCTION

A series of experiments were carried out with both **8** and **11** to study their reactivity in reductive catalytic H_2 evolution. The CVs of **11** in increasing concentrations of deionized (DI) water in ACN remained reversible, with no further increase in the cathodic current relative to the solution in the absence of **11**. On the other hand, upon the addition of 1.0 M of DI water to the ACN, the CVs of **8** show dramatic catalytic current increases (Figure 4a). However, the onset of this catalytic current was observed when a potential of -1.7 V, beyond the Co^{III}/Co^{II} redox couple, was applied (Figure 4c). This suggested the possibility that **8** may just be a pre-catalyst, whereas the active species is formed from its electrochemical transformation.

To elucidate the origin of this unexpected increase in current, different concentrations of water were added and the CVs were analyzed (Figure 4b). As the concentration of water increased from 0 to 0.10 M, both the anodic and cathodic wave currents decreased. This change in redox behavior of **8**, suggested a chemical transformation of the complex in solution under these conditions. Notably, there was no significant increase in the current when a potential beyond -1.7 V was applied at these concentrations of water. However, as the concentration of water was increased to 1.0 M, three new cathodic and two anodic waves were observed, coupled with the dramatic increase in current at -1.7 V (pink line, Figure 4d). These new redox waves are attributed to the formation of new intermediates that arose from water coordination to **8**, and their subsequent chemical transformation during the CV.

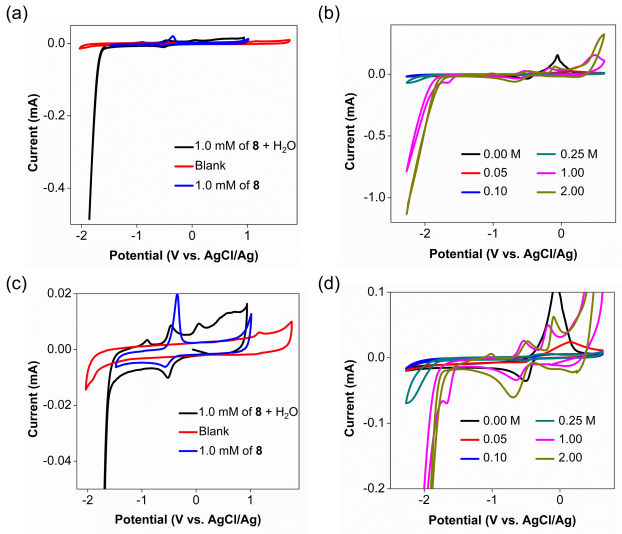

Figure 4. CVs of (a) 1.0 mM of **8** in the absence (blue) and presence (black) of 1.0 M of water in ACN. (b) CVs of 1.0 mM of **8** with different concentrations of water in ACN at scan rates of 100 mV s^{-1}. (c) Expansion of the data in (a) to show the detailed behavior. (d) Expansion of the data in (b) to show the detailed behavior.

Furthermore, a Tafel plot of **8** from the CV measurements gave a slope of 150 mV/decade (Figure 5), which suggests that the rate-determining step for H_2 evolution is likely to be the Volmer reaction ($H^+ + e^- = H_{adsorbed}$).[22] Since this process is typically observed for heterogeneous catalysis, this prompted us to further investigate the role of heterogenous catalysis in this H_2 evolution system. Previous investigations of similar processes have revealed that the active species may in fact be metal oxide or metal nanoparticles, rather than the parent homogeneous complexes that are the active electrocatalyst.[23]

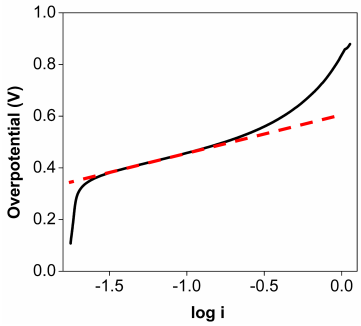

Figure 5. Tafel plot of **8** obtained from the CV measurements in 1.0 M DI water in ACN.

Controlled potential electrolysis (CPE) experiments were then conducted with a glassy carbon electrode to confirm the identity of and quantify the product via gas chromatography (GC). The CPE measurements were performed with the same three-electrode setup as the CV experiments in 1.0 M of DI water in ACN with a glassy carbon rod as the working electrode. A constant potential of –2.0 V was applied for 50 min. Samples of the headspace were removed by a gas-tight syringe and H_2 was identified as the product by GC (Figure S3, SI). Both the current and charge were each plotted as a function of time (Figure 6). The current-time curve indicated that at least two different processes took place during the electrolysis (Figure 6a). We hypothesize that during the first 1300 s, **8** was transformed into a new species, while the current gradually decreased. This was accompanied by the decolorization of **8** in solution. Subsequently, the current stabilized at -4.95 mA until we stopped the CPE experiment at 2500 s, during which a steady current was observed over the span of 1200 s. We postulate that this latter behavior could be a steady rate of H_2 production from the actual heterogeneous catalyst. The UV-vis spectrum taken after the CPE displayed a remarkable loss of absorption in the visible region (Figure S4, SI). Furthermore, based on the amount of H_2 obtained by GC, the Faradaic efficiency for H_2 evolution by **8** after 50 min was calculated to be only 18.2%. Thus, we believe that the lower than quantitative Faradaic efficiency could arise because current was consumed to transform **8** to the active H_2 evolution catalyst during the CPE experiments. As expected, when the CPE was conducted with 1.0 mM of **8** in 1.0 M Na_2SO_4 solutions of DI water, no H_2 was detected above the levels produced by just the glassy carbon electrode alone (Figure S5, SI).

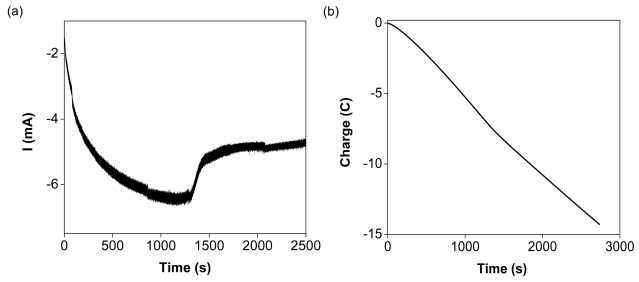

Figure 6. Plots of (a) current and (b) charge against time using 1.0 mM of **8** in ACN (1.0 M of water).

A rinse test was then carried out after the CPE. The same glassy carbon electrode was rinsed with DI water and acetone to wash away residual **8**. It was then used as the working electrode in ACN containing 1.0 M of DI water for a second run. H_2 was detected once again as the electrolysis product. This clearly confirmed that the active species was a heterogeneous catalyst that had been deposited during the first round of electrolysis. The charge consumed within 1300 s of 7.1 C exceeded the charge required for the three-electron reduction of all the Co^{III} TAML in solution to Co^0 (2.3 C), suggesting that **8** may have been completely demetallated by the applied potential of -1.7 V in ACN (1.0 M DI water) during CPE.

High-resolution transmission electron microscopy (HRTEM), energy dispersive X-ray spectroscopy (EDS), and X-ray photoelectron spectroscopy (XPS) were carried out to further investigate the electrodeposited material. The HRTEM images showed nano-sized, non-uniform particles coated on the glassy carbon electrode (Figures 7a and S6). The particles showed lattice *d*-spacings of 0.226 and 0.208 nm corresponding to the (111) and the (200) plane respectively, which are consistent with those of Co^0 nanoparticles (Figure 7d). Furthermore, high-angle annular bright-field-scanning transmission electron microscopy (HAABF-STEM) together with elemental mapping verified the uniform distribution of Co in the sample, with some alumina present, likely from the abrasives used for polishing the carbon electrode (Figure 7).

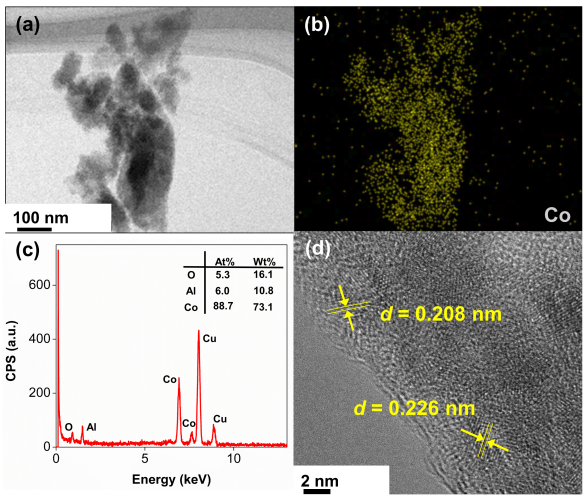

Figure 7. (a) HAABF-STEM of the Co particles. (b) Elemental mapping of Co particles (yellow) and (c) elemental distribution of particles using EDS. (d) lattice fringes with *d*-spacings of 0.226 nm and 0.208 nm corresponding to (111) plane and (200) plane of Co^0 nanoparticles.

The oxidation states and chemical nature of the electrodeposited film was further investigated by XPS experiments. Figure 8a shows the XPS spectrum in the Co 2p window for a sample of the nanoparticulate layer. The peak and shoulder of the Co $2p_{3/2}$ band can be fit to three distinct peaks with binding energies of 779.9, 782.1, and 785.9 eV. These three peaks' binding energies are similar to those of the anhydrous $CoCl_2$ that we used as a reference for materials containing Co^{II} (Figure 8b). For the $CoCl_2$ sample, the two peaks of the Co $2p_{3/2}$ band are fitted with two components at higher binding that could be satellite or shake-up peaks, while the two more components at lower binding energies are consistent with

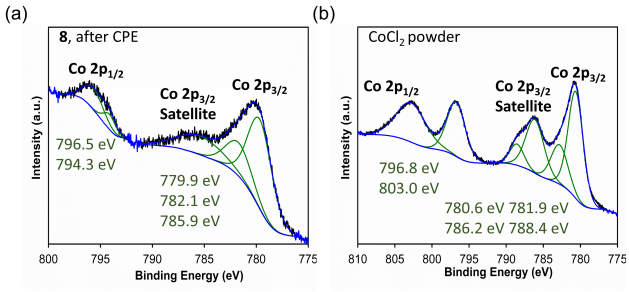

Figure 8. XPS spectra of (a) **8** after CPE and (b) anhydrous $CoCl_2$.

Co^{II} interacting with Cl.[24] By comparing the data from the nanoparticulate film with those from $CoCl_2$, it appeared that there may be some Co^{II} present in the electrodeposited material, likely due to partial oxidation of the surface Co^0 by air.

Since there had been previous reports of electrodeposited Co-based heterogeneous catalysts that were capable of proton reduction in aqueous buffer solutions,[23a] we examined if the Co^0 nanoparticulate film on our electrode had the same properties as those reports. We conducted linear sweep voltammetry experiments on **8** to determine the overpotential of H_2 evolution for the Co^0 nanoparticulate layer in a phosphate buffer solution (KH_2PO_4/K_2HPO_4, 0.50 M, pH = 7.2). However, unlike what Saveant and coworkers observed,[23a] the onset of the catalytic current occurred at a similar potential of -1.1 V, with or without **8**, suggesting that our Co^0 film was distinct from the ones in previous reports (Figure S7). Thus, it appears that there are subtle differences in the nature of the electrodeposited Co^0 heterogeneous catalyst that depend on the choice of the precursor. In our system, the Co^0 nanoparticulate film mainly showed electrocatalytic H_2 evolution activity at intermediate concentrations of water (around 1.0 M).

The disparate electrochemical behavior between **8** and **11**, and also for **8** in different solvents prompted us to consider the electronic structure of the complexes by molecular orbital theory. We propose that the reason may be due to differences in the electronic structures of **8** and **11** when distinct solvent molecules bind, and this hypothesis has been summarized in a Walsh diagram (Figure S8).

CONCLUSION

Late first-row transition metal complexes supported by a new electron-rich TAML ligand were synthesized and characterized by spectroscopic and structural studies. Complex **11** exhibited reversible redox waves, whereas the **8** exhibited a quasi-reversible Co^{III}/Co^{II} redox couple. Both the **8** and **11** were then investigated for electrocatalytic proton reduction activity in aqueous solutions and ACN containing neutral water. Interestingly, **8**, but not **11**, appeared to show electrocatalytic proton reduction, albeit only at intermediate concentrations of water around 1 M. However, upon careful examination, we discovered that an electrodeposited Co^0 nanoparticulate film was responsible for the catalytic activity, as verified by electron microscopy and XPS. We propose that with different concentrations of water, **8** adopted distinct coordination geometries, with the kinetically labile square pyramidal intermediate being more susceptible to demetallation than the low-spin octahedral complex.

EXPERIMENTAL SECTION

MATERIALS AND METHODS

Chemicals were obtained from Sigma-Aldrich, Alfa-Aesar, and Tokyo Chemical Industry Co., Ltd. (TCI). Unless otherwise noted, the commercial reagents were used as purchased. All reactions involving air- or moisture-sensitive compounds were performed by standard Schlenk techniques in oven-dried reaction vessels under an argon atmosphere.

The ^1H and ^{13}C NMR measurements were recorded on Bruker AV-400 (400 MHz) or BBFO-400 (400 MHz) NMR spectrometers. The ^1H and ^{13}C NMR spectra are reported in parts per million (ppm) downfield referenced to the residual protons of the deuterated solvents. UV-visible absorption measurements were carried out on a Shimadzu UV-3600 spectrophotometer. Elemental analyses were performed with an Elementar vario MICRO cube analyser. High-resolution mass spectra (HR-MS) were obtained with a Q-TOF Premier LC HR mass spectrometer.

Cyclic Voltammetry

The controlled-potential coulometric experiments were performed using a Biologic SP-300 potentiostat. A three-electrode electrochemical cell was used with a glassy carbon d to the Ag/AgCl scale using E(NHE) = E(Ag/AgCl) + 0.197 V. Before each experiment, the working electrode (glassy carbon) was polished using a 0.05 μm alumina suspension on a polishing pad, followed by sonication in deionized (DI) water for 10 min, and dried in air. The saturated Ar solutions were prepared by bubbling Ar through the solvents for 30 min.

Scan Rate Dependence Study

In an electrochemical cell, 1.0 mM of **8** or **11** was dissolved in 0.10 M $n\text{-}Bu_4NPF_6$ in ACN (5 mL). CV measurements were collected at various scan rates ranging from 100 mV s^{-1} to 1000 mV s^{-1}.

H_2O Dependence Study

In an electrochemical cell, 1.0 mM of **8** was dissolved in 0.10 M $n\text{-}Bu_4NPF_6$ in ACN by adding 0 − 3.0 M H_2O at various scan rates. Plots of i_c/i_p versus $[H_2O]$ were used to determine the order with respect to the H_2O concentration. In the plot, i_c is the catalytic current and i_p is the peak current observed for the catalyst in the absence of acid.

CPE for the Determination of Faradaic Efficiency, TON and TOF

The CPE measurements performed to calculate the Faradaic efficiency of the catalyst were performed on a CHI 660D work station (CH Instruments. Inc.) with a customized gas-tight, three-neck, 63 mL electrolysis cell. A glassy carbon rod was employed as the working electrode, while a platinum coil counter electrode and an Ag/AgCl reference electrode were placed in the electrolyte solution. The electrolysis was carried out at an applied potential of -2.0 V. The solution was constantly stirred during the electrolysis experiments. Gas samples were taken from the headspace of the cell and injected into an Agilent 7890A gas-chromatograph/and a Shimadzu gas chromatograph GC-2010 (with a thermal conductivity detector, a 5 Å molecular sieve column (2 mm x 5 m), and Ar as the carrier gas). The amount of H_2 was quantified by a GC calibration curve derived by using H_2 samples of known concentration. The amount of H_2 generated from the electrolysis experiments and the amount of consumed charge of each CPE experiment were calculated based on the following equations:

$$TON = n_{hydrogen}/n_{cat} \text{ (mol } H_2 \text{ per mol catalyst)}$$

TOF = TON/ (duration of electrolysis) (mol H_2 per mol catalyst per hour)

The $n_{hydrogen}$ is the number of moles of H_2 generated from the electrolysis, and n_{cat} is the number of moles of catalyst used in the electrolysis experiment.

The Faradaic efficiency was calculated as follows:

$$\text{Faradaic efficiency for } H_2 = (2xF / Q) \times 100\%$$

The total amount of charge (Q) passed through the cell was obtained from the charge-time curve. The total amount of H_2 produced (x) was measured by a GC. Since two electrons are needed to make one H_2 molecule from two protons, there is a coefficient of 2 in the numerator.

Materials Characterization

Transmission Electron Microscopy (TEM)

The morphology and structure of the samples were characterized by TEM with a JEOL JEM-1400 operated at 100 kV and a high-resolution TEM (HRTEM) with a JEOL JEM-2100F operated at 200 kV. The HRTEM is equipped with a scanning transmission electron microscope (STEM) and an energy-dispersive X-ray spectrometer for STEM images and elemental analysis, respectively. The sample preparation involved sonicating an aliquot of the electrodeposited material on the electrode in analytical-grade ethanol for 10 min. A single drop of the colloidal solution was dropped on a thin, lacey, carbon-coated copper TEM grid and dried in air. This TEM grid was then used in the imaging experiments.

Field Emission Scanning Electron Microscopy (FESEM)

The FESEM equipped with an energy-dispersive X-ray spectrometer was used to examine the samples using a JEOL JSM-7600F operated at 5 kV. Each sample was prepared by coating a uniform layer of the materials on SPI double-sided adhesive carbon tape and mounted on an aluminum (Al) SEM specimen stub.

X-ray Photoelectron Spectroscopy (XPS)

XPS experiments were performed using a Phoibos 100 spectrometer and a Mg X-ray source (SPECS, Germany) working at 12.5 kV equipped with dual Al/Mg anodes. XPS measurements were performed on solid powder samples pressed onto SPI double-sided adhesive carbon tape. The XPS data obtained were processed using the CasaXPS software. The spectra were calibrated internally by setting the C 1s signal at 284.6 eV.

Synthesis of 2,4-diazido-2,4-dimethylpentanone (2):

This compound was synthesized according to the procedure described by Collins and coworkers.[13f] To a solution of 2,4-dibromo-2,4-dimethylpentanone (**2**) (4.49 g, 16.5 mmol) in ethanol (60 mL) was added a solution of NaN_3 (2.36 g, 36.3 mmol, 2.2 equiv.) in water (30 mL). The solution was heated under reflux (external temperature set at 94 °C) for 16 h to give pale yellow solution. The ethanol was removed under reduced pressure until the solution turned cloudy. The solution was then extracted with n-pentane (3 x 25 mL), dried over Na_2SO_4, and concentrated under reduced pressure. This concentrated solution was used in the next step without further purification due to concerns over the safety of isolating large amounts of this organic aliphatic azide. ^{1}H NMR (300 MHz, $CDCl_3$): 1.86 (s, 12 H) ppm. HRMS (ESI+, m/z) calculated for $C_7H_{13}N_6O$ $[M + H]^+$ m/z = 197.1151, found 197.1159.

Synthesis of 2,4-diamino-2,4-dimethylpentan-3-ol (3):

A 100 mL Schlenk flask was charged with anhydrous THF (45 mL) and $LiAlH_4$ (1.37 g, 36.0 mmol) under a nitrogen atmosphere. The mixture was cooled to –10 °C and the concentrated solution of **2**, obtained in the previous step, was added slowly under a N_2 positive pressure. The resulting mixture's temperature was maintained below 0 °C and was stirred for 30 min. Subsequently, the mixture was warmed to room temperature and stirred for another 24 h. The mixture was then cooled in an ice bath at –5 °C and the $LiAlH_4$ was quenched by addition of aqueous NaOH solution (10%). The supernatant was decanted into a round bottom flask and the residue in the Schlenk flask was extracted with ethyl acetate (3 x 10 mL). The combined organic extracts were dried over Na_2SO_4 and the solvents were removed under reduced pressure. The viscous colorless oil thus obtained was dissolved in CHC_{l3} and dried over Na_2SO_4. The solvent was removed under reduced pressure, and the residue was further dried under high vacuum until colorless crystals formed (1.92 g, 13.1 mmol, 79.6%). ^{1}H NMR (300 MHz, DMSO-d_6): 1.07 (s, 6 H), 1.08 (s, 6 H), 2.82 (s, 1 H) ppm. ^{13}C[17a] NMR (75 MHz, DMSO-d_6): 29.25, 29.74, 53.85, 82.46 ppm. HRMS (ESI+, m/z) calculated for $C_7H_{19}N_2O$ $[M + H]^+$ m/z = 147.1497, found 147.1498. Elemental analyses for $C_7H_{18}N_2O$ calculated: C, 57.49; H, 12.41; N, 19.16%; found: C, 57.38; H, 12.52; N, 19.10%.

Synthesis of bis-2,4-(2-bromo-2-methylpropanamido)-2,4-dimethylpentan-3-ol (4):

To a 100 mL Schlenk flask, **3** (1.25 g, 8.55 mmol), triethylamine (TEA, 2.00 g, 19.8 mmol), and DCM (30 mL) were added under a N_2 atmosphere at room temperature. The solution was cooled to 0 °C and α-bromoisobutyryl bromide (4.13 g, 18.0 mmol) was syringed in dropwise. The reaction is very exothermic and the reagent should be added in very carefully to avoid boiling the solvent. After complete addition, the reaction mixture was stirred for 30 min at 0 °C. The dichloromethane was then removed under reduced pressure and the white solid thus obtained was dissolved in ethyl acetate (20 mL) and washed with brine (2 x 10 mL). The organic phase was dried over Na_2SO_4 and concentrated under reduced pressure. The obtained white solid was transferred to a frit, washed with hexane (5 x 5 mL), and dried under vacuum, yielding a white solid product (3.34 g, 7.53 mmol, 88.1 %). ^{1}H NMR (400 MHz, $CDCl_3$): 1.48 (s, 6 H), 1.50 (s, 6 H), 1.92 (d, J = 2 Hz, 12 H), 3.94 (s, 1 H), 5.29 (s, 1 H), 6.93 (s, 2 H) ppm. ^{13}C[23a] NMR (100 MHz, $CDCl_3$): 25.70, 25.79, 32.51, 32.57, 59.31, 63.31, 79.51, 172.28 ppm. HRMS (ESI+, m/z) calculated for $C_{15}H_{29}Br_2N_2O_3$ $[M + H]^+$ m/z = 443.0545, found 443.0540. Elemental analyses for $C_{15}H_{28}Br_2N_2O_3$ calculated: C, 40.56; H, 6.35; N, 6.31%; found: C, 40.93; H, 6.58; N, 5.98%.

Synthesis of bis-2,4-(2-azido-2-methylpropanamido)-2,4-dimethylpentan-3-ol (5):

To a solution of 4 (3.31 g, 7.45 mmol) in ethanol (60 mL) was added a solution of NaN_3 (2.91 g, 44.7 mmol, 6.0 equiv.) in water (20 mL). The solution was heated at 78 °C for 36 h. The ethanol was removed under reduced pressure and the reaction mixture was extracted with DCM (3 x 15 mL) and dried over Na_2SO_4. The

DCM was removed under reduced pressure and the remaining viscous oil was further dried under vacuum until it became colorless crystals (2.71 g, 7.36 mmol, 98.8%). ^{1}H NMR (300 MHz, $CDCl_3$): 1.42 (s, 6 H), 1.45 (s, 6 H), 1.49 (s, 6 H), 1.49 (s, 6 H), 3.87 (d, J = 7.8 Hz, 1 H), 5.70 (d, J = 8.0 Hz, 1 H), 6.69 (s, 2 H) ppm. ^{13}C{^{1}H} NMR (75 MHz, $CDCl_3$): 24.41, 24.48, 25.96, 26.05, 58.96, 64.59, 79.64, 172.61 ppm. HRMS (ESI+, m/z) calculated for $C_{15}H_{29}N_8O_3$ [M + H]+ m/z = 369.2363, found 369.2361. Elemental analyses for $C_{15}H_{28}N_8O_3$ calculated: C, 48.90; H, 7.66; N, 30.41%; found: C, 48.99; H, 7.41; N, 30.24%.

Synthesis of bis-2,4-(2-amino-2-methylpropanamido)-2,4-dimethylpentan-3-ol (6):

Red-Al (70% in toluene, 3.29 g, 16.3 mmol, 6 equiv.) was added dropwise to a solution of **5** (1.00 g, 2.71 mmol) in dry THF (20 mL) over 30 min under a N_2 atmosphere at –10 °C and stirred for an additional 3 h. The excess Red-Al was quenched with NaOH (10% aqueous solution, 20 mL). The supernatant was decanted and the solvent was removed under reduced pressure. The oily residue was dissolved in ethyl acetate (15 mL) and extracted with 1 M HCl (3 x 10 mL). The combined aqueous extracts were neutralized with Na_2CO_3 and dried under reduced pressure. The residue was subsequently extracted with chloroform (3 x 10 mL). The combined chloroform extracts were dried over Na_2SO_4, filtered, and the filtrate was concentrated by rotary evaporation. Additional drying in vacuo yielded a colorless solid (0.80 g, 2.53 mmol, 93.4%). ^{1}H NMR (500 MHz, $CDCl_3$): 1.32 (s, 6 H), 1.33 (s, 6 H), 1.43 (s, 6 H), 1.47 (s, 6 H), 3.86 (s, 1 H), 6.40 (s, 1 H), 7.95 (s, 2 H) ppm. ^{13}C{^{1}H} NMR (126 MHz, $CDCl_3$): 25.95, 26.38, 29.12, 29.17, 55.11, 58.28, 80.27, 177.96 ppm. HRMS (ESI+, m/z) calculated for $C_{15}H_{33}N_4O_3$ [M + H]+ m/z = 317.2553, found 317.2561. Elemental analyses for $C_{15}H_{32}N_4O_3$ calculated: C, 56.93; H, 10.19; N, 17.71%; found: C, 56.77; H, 10.21; N, 17.53%.

Synthesis of TAML (7):

To a 200 mL Schlenk flask, **6** (0.200 g, 0.63 mmol), anhydrous TEA (0.185 mL, 0.134 g, 1.32 mmol) and anhydrous THF (140 mL) were added under nitrogen at room temperature. The solution was cooled to –10 °C and a solution of 2,2-dimethylmalonyl chloride (0.083 mL, 0.107 g, 0.630 mmol) in anhydrous THF (60 mL) was added dropwise over 8 h by a dropping funnel. The reaction temperature was increased to 25 °C and the mixture was stirred for another 5 h. Subsequently, the solvent was removed by rotary evaporation. The white residue was suspended in $CHCl_3$ (30 mL), washed with 10% aqueous brine (3 x 15 mL), dried over Na_2SO_4, and the solvent was removed by rotary evaporation. The white residue was purified by silica gel column chromatography (ethyl acetate as the solvent) to yield TAML (0.150 g, 0.360 mmol, 57.1%). ^{1}H NMR (500 MHz, $CDCl_3$): 1.31 (s, 6 H), 1.46 (s, 6 H), 1.51 (s, 6 H), 1.52 (s, 6 H), 1.54 (s, 3 H), 1.54 (s, 3 H), 3.53 (s, 1 H), 6.14 (s, 2 H), 6.34 (s, 2H) ppm. ^{13}C{^{1}H} NMR (126 MHz, $CDCl_3$): 20.62, 20.90, 25.81, 29.54, 52.41, 57.95, 58.46, 82.75, 171.49, 173.93 ppm. HRMS (ESI+, m/z) calculated for $C_{20}H_{37}N_4O_5$ $[M + H]^+$ m/z = 413.2764, found 413.2761. Elemental analyses for $C_{20}H_{36}N_4O_5$ calculated: C, 58.23; H, 8.80; N, 13.58%; found: C, 58.28; H, 9.16; N, 13.96%.

Synthesis of 8:

Solutions of **7** (25.0 mg, 0.060 mmol) in 5 mL anhydrous THF was added to a solution of LiHMDS (45.2 mg, 0.27 mmol, 4.5 equiv.) in 5 mL anhydrous THF in a 25 mL Schlenk flask under N_2 at room temperature. The mixture was stirred for 15 min before $CoCl_2$ (7.81 mg, 0.060 mmol) was added. The mixture became dark purple within 30 min. The reaction mixture was then stirred for another 2 h. The solvent was removed by rotary evaporation and the residue was washed with DCM (3 x 10 mL), followed by pentane (3 x 5 mL). The residue was then dried under vacuum. The dark red solid was suspended in THF (10 mL) and filtered. The dark red filtrate was dried in vacuo to yield the desired product (26.4 mg, 0.060 mmol, 91.6%).

Synthesis of 9:

A solution of **7** (50.0 mg, 0.12 mmol) in 10 mL anhydrous THF was added to a solution of lithium hexamethyldisilazide (LiHMDS, 90.4 mg, 0.54 mmol, 4.5 equiv.) in 5 mL anhydrous THF in a 25 mL Schlenk flask under N_2 at room temperature. The mixture was stirred for 15 min under N_2. $(PPh_3)_2NiBr_2$ (89.2 mg, 0.12 mmol) was added and the mixture became a pale orange solution within 5 min. The solvent was removed under reduced pressure and the residue was washed with DCM (3 x 10 mL), followed by ACN (3 x 5 mL). The pale orange solid obtained was dissolved in methanol (15 mL), filtered, and the filtrate was dried under reduced pressure to yield **9** (55.8 mg, 0.12 mmol, 96.4%).%). ^{1}H NMR (300 MHz, MeOD): 1.33 (s, 6 H), 1.39 (s, 6 H), 1.47 (s, 6 H), 1.48 (s, 6 H), 1.61 (s, 3 H), 1.73 (s, 3 H), 2.88 (s, 1 H) ppm. HRMS (ESI+, m/z) calculated for $C_{20}H_{35}N_4NiO_5$ $[M + 3H]^+$ m/z = 369.1961, found 369.1956. $[(TAML)Ni]^{2-}$: HRMS (ESI-, m/z) calculated for $C_{20}H_{33}N_4NiO_5$ $[M + H]^-$ m/z = 467.1804, found 467.1810 Elemental analyses for $C_{20}H_{32}Li_2NiN_4O_5$ calculated: C, 49.93; H, 6.71; N, 11.65%; found: C, 50.16; H, 6.70; N, 11.47%.

Synthesis of 10:

Complex **8** (8.00 mg, 0.017 mmol) was dissolved in 3 mL of water with Et_4NF (15.0 mg, 0.10 mmol, 6 equiv.) and stirred for 12 h. The water was removed under reduced pressure and the solid dark red residue was dissolved in DCM (5 mL). The DCM was removed under reduced pressure to give a deep red powder. (9.5 mg, 0.015 mmol, 93.2%). Vapor diffusion of diethyl ether into DCM gave deep red crystals suitable for XRD. Elemental analyses for $C_{28}H_{52}CoN_5O_5$ calculated: C, 56.27; H, 8.77; N, 11.72%; found: C, 56.52; H, 8.85; N, 11.52%. HRMS (ESI-, m/z) calculated for $C_{20}H_{32}N_4CoO_5$ $[M]^-$ m/z = 467.1705, found 467.1703.

Synthesis of 11:

Complex **9** (8.00 mg, 0.017 mmol) was dissolved in 3 mL of water. Et_4NF (15.0 mg, 0.10 mmol, 6 equiv.) was added and the reaction mixture was stirred for 12 h. The solvent was removed under reduced pressure and the residue was suspended in DCM (5 mL). The mixture was filtered, and the filtrate was dried by rotary evaporation to give **11** (10.2 mg, 0.014 mmol, 87.8%).%). ^{1}H NMR (300 MHz, MeOD): 1.37 (s, 6 H), 1.37 (s, 6 H), 1.48 (s, 6 H), 1.48 (s, 6 H), 1.62 (s, 3 H), 1.69 (s, 3 H), 1.88 (s, 1 H), 2.02 (s, 1 H) ppm. HRMS (ESI-, m/z) calculated for $C_{20}H_{33}N_4NiO_5$ $[M + H]^-$ m/z = 467.1804, found 467.1810. Elemental analyses for $C_{36}H_{72}N_6NiO_5$ calculated: C, 59.42; H, 9.97; N, 11.55%; found: C, 59.21; H, 10.14; N, 11.32%.

ASSOCIATED CONTENT

SUPPORTING INFORMATION

The Supporting Information is available free of charge via the internet at http://pubs.acs.org.

Additional electrochemistry data, NMR spectroscopic characterization of the ligands and complexes, and essential crystallographic data (PDF).

X- ray crystallographic data of **8** deposited under CCDC 1857749 (CIF).

AUTHOR INFORMATION

Corresponding Author

* Email: hansen@ntu.edu.sg; Tel: +65 65923182.

Notes

The authors declare no competing financial interest.

ACKNOWLEDGMENT

H.S.S. is supported by MOE Tier 1 grants RG 12/16 and RG 13/17. H.S.S. also acknowledges the Agency for Science, Technology and Research (A*STAR), AME IRG grant A1783c0002 for funding this research. The authors are grateful for support from the Solar Fuels Lab at NTU.

REFERENCES

(1) (a) Jin, H.; Guo, C.; Liu, X.; Liu, J.; Vasileff, A.; Jiao, Y.; Zheng, Y.; Qiao, S.-Z., Emerging Two-Dimensional Nanomaterials for Electrocatalysis. *Chem. Rev.* **2018,** *118*, 6337-6408; (b) Tao, H. C.; Gao, Y. A.; Talreja, N.; Guo, F.; Texter, J.; Yan, C.; Sun, Z. Y., Two-dimensional nanosheets for electrocatalysis in energy generation and conversion. *J. Mater. Chem. A* **2017,** *5*, 7257-7284; (c) Mistry, H.; Varela, A. S.; Kuhl, S.; Strasser, P.; Cuenya, B. R., Nanostructured electrocatalysts with tunable activity and selectivity. *Nat. Rev. Mater.* **2016,** *1*, 1-14.

(2) (a) Savéant, J.-M., Molecular Catalysis of Electrochemical Reactions. Mechanistic Aspects. *Chem. Rev.* **2008,** *108*, 2348-2378; (b) Vincent, K. A.; Parkin, A.; Armstrong, F. A., Investigating and exploiting the electrocatalytic properties of hydrogenases. *Chem. Rev.* **2007,** *107*, 4366-4413; (c) Costentin, C.; Robert, M.; Savéant, J.-M., Concerted Proton– Electron Transfers: Electrochemical and Related Approaches. *Acc. Chem. Res.* **2010,** *43*, 1019-1029; (d) Rakowski Dubois, M.; Dubois, D. L., Development of Molecular Electrocatalysts for CO_2 Reduction and H_2 Production/Oxidation. *Acc. Chem. Res.* **2009,** *42*, 1974-1982.

(3) (a) Francke, R.; Schille, B.; Roemelt, M., Homogeneously Catalyzed Electroreduction of Carbon Dioxide-Methods, Mechanisms, and Catalysts. *Chem. Rev.* **2018,** *118*, 4631-4701; (b) Nutting, J. E.; Rafiee, M.; Stahl, S. S., Tetramethylpiperidine N-Oxyl (TEMPO), Phthalimide N-Oxyl (PINO), and Related N-Oxyl Species: Electrochemical Properties and Their Use in Electrocatalytic Reactions. *Chem. Rev.* **2018,** *118*, 4834-4885; (c) Yan, M.; Kawamata, Y.; Baran, P. S., Synthetic Organic Electrochemical Methods Since 2000: On the Verge of a Renaissance. *Chem. Rev.* **2017,** *117*, 13230-13319.

(4) Dokic, M.; Soo, H. S., Artificial Photosynthesis by Light Absorption, Charge Separation, and Multielectron Catalysis. *Chem. Commun.* **2018,** *54*, 6554-6572.

(5) (a) Faunce, T. A.; Lubitz, W.; Rutherford, A. W.; MacFarlane, D. R.; Moore, G. F.; Yang, P. D.; Nocera, D. G.; Moore, T. A.; Gregory, D. H.; Fukuzumi, S.; Yoon, K. B.; Armstrong, F. A.; Wasielewski, M. R.; Styring, S., Energy and environment policy case for a global project on artificial photosynthesis. *Energy Environ. Sci.* **2013,** *6*, 695-698; (b) Khaselev, O.; Turner, J. A., A monolithic photovoltaic-photoelectrochemical device for hydrogen production via water splitting. *Science* **1998,** *280*, 425-427; (c) Lewis, N. S.; Nocera, D. G., Powering the planet: Chemical challenges in solar energy utilization. *Proc. Natl. Acad. Sci. U.S.A.* **2006,** *103*, 15729-15735.

(6) (a) Pu, Z. H.; Amiinu, I. S.; Kou, Z. K.; Li, W. Q.; Mu, S. C., RuP2-Based Catalysts with Platinum-like Activity and Higher Durability for the Hydrogen Evolution Reaction at All pH Values. *Angew. Chem. Int. Ed.* **2017,** *56*, 11559-11564; (b) Seh, Z. W.; Kibsgaard, J.; Dickens, C. F.; Chorkendorff, I. B.; Norskov, J. K.; Jaramillo, T. F., Combining theory and experiment in electrocatalysis: Insights into materials design. *Science* **2017,** *355*.

(7) (a) Thoi, V. S.; Sun, Y. J.; Long, J. R.; Chang, C. J., Complexes of earth-abundant metals for catalytic electrochemical hydrogen generation under aqueous conditions. *Chem. Soc. Rev.* **2013,** *42*, 2388-2400; (b) Zee, D. Z.; Chantarojsiri, T.; Long, J. R.; Chang, C. J., Metal-Polypyridyl Catalysts for Electro- and Photochemical Reduction of Water to Hydrogen. *Acc. Chem. Res.* **2015,** *48*, 2027-2036; (c) Chen, L.; Wang, M.; Han, K.; Zhang, P. L.; Gloaguen, F.; Sun, L. C., A super-efficient cobalt catalyst for electrochemical hydrogen production from neutral water with 80 mV overpotential. *Energy Environ. Sci.* **2014,** *7*, 329-334; (d) Helm, M. L.; Stewart, M. P.; Bullock, R. M.; DuBois, M. R.; DuBois, D. L., A Synthetic Nickel Electrocatalyst with a Turnover Frequency Above 100,000 s^{-1} for H_2 Production. *Science* **2011,** *333*, 863-866; (e) Koshiba, K.; Yamauchi, K.; Sakai, K., A Nickel Dithiolate Water Reduction Catalyst Providing Ligand-Based Proton-Coupled Electron-Transfer Pathways. *Angew. Chem. Int. Ed.* **2017,** *56*, 4247-4251; (f) Shao, H.; Muduli, S. K.; Tran, P. D.; Soo, H. S., Enhancing Electrocatalytic Hydrogen Evolution by Nickel Salicylaldimine Complexes with Alkali Metal Cations in Aqueous Media. *Chem. Commun.* **2016,** *52*, 2948-2951.

(8) (a) Sherbow, T. J.; Fettinger, J. C.; Berben, L. A., Control of Ligand pK(a) Values Tunes the Electrocatalytic Dihydrogen Evolution Mechanism in a Redox-Active Aluminum(III) Complex. *Inorg. Chem.* **2017,** *56*, 8651-8660; (b) Thompson, E. J.; Berben, L. A., Electrocatalytic Hydrogen Production by an Aluminum(III) Complex: Ligand-Based Proton and Electron Transfer. *Angew. Chem. Int. Ed.* **2015,** *54*, 11642-11646.

(9) (a) Halter, D. P.; Heinemann, F. W.; Bachmann, J.; Meyer, K., Uranium-mediated electrocatalytic dihydrogen production from water. *Nature* **2016,** *530*, 317-321; (b) Halter, D. P.; Heinemann, F. W.; Maron, L.; Meyer, K., The role of uranium-arene bonding in H2O reduction catalysis. *Nat. Chem.* **2018,** *10*, 259-267; (c) Halter, D. P.; Palumbo, C. T.; Ziller, J. W.; Gembicky, M.; Rheingold, A. L.; Evans, W. J.; Meyer, K., Electrocatalytic H2O Reduction with f-Elements: Mechanistic Insight and Overpotential Tuning in a

Series of Lanthanide Complexes. *J. Am. Chem. Soc.* **2018,** *140*, 2587-2594.
(10) Chen, H.; Sun, Z.; Ye, S.; Lu, D.; Du, P., Molecular cobalt–salen complexes as novel cocatalysts for highly efficient photocatalytic hydrogen production over a CdS nanorod photosensitizer under visible light. *J. Mater. Chem. A* **2015,** *3*, 15729-15737.
(11) (a) DuBois, M. R.; DuBois, D. L., The roles of the first and second coordination spheres in the design of molecular catalysts for H 2 production and oxidation. *Chem. Soc. Rev.* **2009,** *38*, 62-72; (b) Helm, M. L.; Stewart, M. P.; Bullock, R. M.; DuBois, M. R.; DuBois, D. L., A Synthetic Nickel Electrocatalyst with a Turnover Frequency Above 100,000 s^{-1} for H_2 Production. *Science* **2011,** *333*, 863-866; (c) Bang, S.; Lee, Y. M.; Hong, S.; Cho, K. B.; Nishida, Y.; Seo, M. S.; Sarangi, R.; Fukuzumi, S.; Nam, W., Redox-inactive metal ions modulate the reactivity and oxygen release of mononuclear non-haem iron(III)-peroxo complexes. *Nat. Chem.* **2014,** *6*, 934-940; (d) Dubois, M. R.; Dubois, D. L., Development of Molecular Electrocatalysts for CO_2 Reduction and H_2 Production/Oxidation. *Acc. Chem. Res.* **2009,** *42*, 1974-1982; (e) Tsui, E. Y.; Tran, R.; Yano, J.; Agapie, T., Redox-inactive metals modulate the reduction potential in heterometallic manganese-oxido clusters. *Nat. Chem.* **2013,** *5*, 293-299.
(12) (a) Das, S. P.; Ganguly, R.; Li, Y.; Soo, H. S., Nucleophilic Reactivity and Electrocatalytic Reduction of Halogenated Organic Compounds by Nickel o-Phenylenedioxamidate Complexes. *Dalton Trans.* **2016,** *45*, 13556-13564; (b) Gazi, S.; Đokić, M.; Moeljadi, A. M. P.; Ganguly, R.; Hirao, H.; Soo, H. S., Kinetics and DFT Studies of Photoredox Carbon–Carbon Bond Cleavage Reactions by Molecular Vanadium Catalysts under Ambient Conditions. *ACS Catal.* **2017,** *7*, 4682-4691; (c) Gazi, S.; Ng, W. K. H.; Ganguly, R.; Moeljadi, A. M. P.; Hirao, H.; Soo, H. S., Selective photocatalytic C–C bond cleavage under ambient conditions with earth abundant vanadium complexes. *Chem. Sci.* **2015,** *6*, 7130-7142; (d) Ghosh, D.; Febriansyah, B.; Gupta, D.; Ng, L. K.-S.; Xi, S.; Du, Y.; Baikie, T.; Dong, Z.; Soo, H. S., Hybrid Nanomaterials with Single-Site Catalysts by Spatially Controllable Immobilization of Nickel Complexes via Photoclick Chemistry for Alkene Epoxidation. *ACS Nano* **2018,** *12*, 5908-5912; (e) Kee, J. W.; Ng, Y. Y.; Kulkarni, S. A.; Xu, K.; Ganguly, R.; Lu, Y.; Hirao, H.; Soo, H. S., Development of Bis(arylimino)acenaphthene (BIAN) Copper Complexes as Visible Light Harvesters for Potential Photovoltaic Applications. *Inorg. Chem. Front.* **2016**, 651-662; (f) Lim, J. H.; Engelmann, X.; Corby, S.; Ganguly, R.; Ray, K.; Soo, H. S., C-H Activation and Nucleophilic Substitution in a Photochemically Generated High Valent Iron Complex. *Chem. Sci.* **2018,** *9*, 3992-4002; (g) Ho, X. L.; Shao, H.; Ng, Y. Y.; Ganguly, R.; Lu, Y.; Soo, H. S., Visible Light Driven Hydrogen Evolution by Molecular Nickel Catalysts with Time-Resolved Spectroscopic and DFT Insights. *Inorg. Chem.* **2019,** *58*, 1469-1480.
(13) (a) Bartos, M. J.; Gordon-Wylie, S. W.; Fox, B. G.; James Wright, L.; Weintraub, S. T.; Kauffmann, K. E.; Münck, E.; Kostka, K. L.; Uffelman, E. S.; Rickard, C. E. F.; Noon, K. R.; Collins, T. J., Designing ligands to achieve robust oxidation catalysts. Iron based systems. *Coord. Chem. Rev.* **1998,** *174*, 361-390; (b) Bartos, M. J.; Kidwell, C.; Kauffmann, K. E.; Gordon-Wylie, S. W.; Collins, T. J.; Clark, G. C.; Münck, E.; Weintraub, S. T., A stable aquairon(III) complex with S = 1: structure and spectroscopic properties. *Angew. Chem. Int. Ed. Engl.* **1995,** *34*, 1216-1219; (c) Chanda, A.; Popescu, D. L.; Tiago de Oliveira, F.; Bominaar, E. L.; Ryabov, A. D.; Munck, E.; Collins, T. J., High-valent iron complexes with tetraamido macrocyclic ligands: structures, Mossbauer spectroscopy, and DFT calculations. *J Inorg Biochem* **2006,** *100*, 606-19; (d) Collins, T. J., TAML oxidant activators: a new approach to the activation of hydrogen peroxide for environmentally significant problems. *Acc. Chem. Res.* **2002,** *35*, 782-790; (e) Collins, T. J.; Kostka, K. L.; Munck, E.; Uffelman, E. S., Stabilization of mononuclear five-coordinate iron(IV). *J. Am. Chem. Soc.* **1990,** *112*, 5637-5639; (f) Collins, T. J.; Kostka, K. L.; Uffelman, E. S.; Weinberger, T. L., Design, Synthesis, and Structure of a Macrocyclic Tetraamide That Stabilizes High-Valent Middle and Later Transition-Metals. *Inorg. Chem.* **1991,** *30*, 4204-4210; (g) Ellis, W. C.; Tran, C. T.; Denardo, M. A.; Fischer, A.; Ryabov, A. D.; Collins, T. J., Design of more powerful iron-TAML peroxidase enzyme mimics. *J. Am. Chem. Soc.* **2009,** *131*, 18052-18053; (h) Ellis, W. C.; Tran, C. T.; Roy, R.; Rusten, M.; Fischer, A.; Ryabov, A. D.; Blumberg, B.; Collins, T. J., Designing green oxidation catalysts for purifying environmental waters. *J. Am. Chem. Soc.* **2010,** *132*, 9774-9781.
(14) (a) Khetan, S. K.; Collins, T. J., Human Pharmaceuticals in the Aquatic Environment: A Challenge to Green Chemistry. *Chem. Rev.* **2007,** *107*, 2319-2364; (b) Sen Gupta, S.; Stadler, M.; Noser, C. A.; Ghosh, A.; Steinhoff, B.; Lenoir, D.; Horwitz, C. P.; Schramm, K. W.; Collins, T. J., Rapid total destruction of chlorophenols by activated hydrogen peroxide. *Science* **2002,** *296*, 326-328.
(15) Kundu, S.; Chanda, A.; Khetan, S. K.; Ryabov, A. D.; Collins, T. J., TAML activator/peroxide-catalyzed facile oxidative degradation of the persistent explosives trinitrotoluene and trinitrobenzene in micellar solutions. *Environ. Sci. Technol.* **2013,** *47*, 5319-26.
(16) (a) Demeter, E. L.; Hilburg, S. L.; Washburn, N. R.; Collins, T. J.; Kitchin, J. R., Electrocatalytic oxygen evolution with an immobilized TAML activator. *J. Am. Chem. Soc.* **2014,** *136*, 5603-5606; (b) Panda, C.; Debgupta, J.; Díaz Díaz, D.; Singh, K. K.; Sen Gupta, S.; Dhar, B. B., Homogeneous photochemical water oxidation by biuret-modified Fe-TAML: evidence of $Fe^{V}(O)$ intermediate. *J. Am. Chem. Soc.* **2014,** *136*, 12273-12282.
(17) (a) Hong, S.; Pfaff, F. F.; Kwon, E.; Wang, Y.; Seo, M. S.; Bill, E.; Ray, K.; Nam, W., Spectroscopic Capture and Reactivity of a Low-Spin Cobalt(IV)-Oxo Complex Stabilized by Binding Redox-Inactive Metal Ions. *Angew. Chem. Int. Ed.* **2014,** *53*, 10403-10407; (b) Chandra, S.; Gupta, L. K., Spectroscopic approach in characterization of chromium(III), manganese(II), iron(III) and copper(II) complexes with a nitrogen donor tetradentate, 14-membered azamacrocyclic ligand. *Spectrochim. Acta, Part A* **2005,** *61*, 2139-2144; (c) Collins, T. J.; Nichols, T. R.; Uffelman, E. S., A Square-Planar Nickel(Iii) Complex of an Innocent Ligand System. *J. Am. Chem. Soc.* **1991,** *113*, 4708-4709; (d) Comba, P.; Kubeil, M.; Pietzsch, J.; Rudolf, H.; Stephan, H.; Zarschler, K., Bispidine Dioxotetraaza Macrocycles: A New Class of Bispidines for Cu-64 PET Imaging. *Inorg. Chem.* **2014,** *53*, 6698-6707; (e) Salavati-Niasari, M.; Abdolmohammadi, S., Synthesis, characterization and catalytic oxidation of ethylbenzene over "neat" and host (nanocavity of zeolite-Y)/guest (tetraza tetraone macrocyclic copper(II) complexes)

nanocomposite materials (HGNM). *J. Porous Mater.* **2009,** *16*, 19-26; (f) Sangeetha, J. E.; Meenalochani, S.; Radha, K.; Chellappa, D., Synthesis and characterization of transition metal complexes of 12-and 14-membered tetraaza macrocycles. *Asian J. Chem.* **2008,** *20*, 4749-4754; (g) Uffelman, E. S.; Doherty, J. R.; Schulze, C.; Burke, A. L.; Bonnema, K. R.; Watson, T. T.; Lee, D. W., Microscale syntheses, reactions, and H-1 NMR spectroscopic investigations of square planar macrocyclic tetraamido-N Cu(III) complexes relevant to green chemistry. *J. Chem. Educ.* **2004,** *81*, 182-185; (h) Volov, A. N.; Zamilatskov, I. A.; Chernyshev, V. V.; Savinkina, E. V.; Chuvaev, V. F.; Kurochkina, N. M.; Tsivadze, A. Y., Cobalt(II), nickel(II), and copper(II) complexes of 14-membered hexaazamacrocycles: synthesis and characterization. *J. Coord. Chem.* **2014,** *67*, 3121-3134; (i) Wang, H. X.; Butorin, S. M.; Young, A. T.; Guo, J. H., Nickel Oxidation States and Spin States of Bioinorganic Complexes from Nickel L-edge X-ray Absorption and Resonant Inelastic X-ray Scattering. *J. Phys. Chem. C* **2013,** *117*, 24767-24772; (j) Collins, T. J.; Uffelman, E. S., The First Macrocyclic Square - Planar Cobalt(III) Complex Relieves Ring Strain by Forming a Nonplanar Amide. *Angew. Chem., Int. Ed. Engl.* **1989,** *28*, 1509-1511.

(18) Ghosh, A.; Ramidi, P.; Pulla, S.; Sullivan, S. Z.; Collom, S. L.; Gartia, Y.; Munshi, P.; Biris, A. S.; Noll, B. C.; Berry, B. C., Cycloaddition of CO2 to Epoxides Using a Highly Active Co(III) Complex of Tetraamidomacrocyclic Ligand. *Catal. Lett.* **2010,** *137*, 1-7.

(19) Collins, T. J.; Powell, R. D.; Slebodnick, C.; Uffelman, E. S., Stable Highly Oxidizing Cobalt Complexes of Macrocyclic Ligands. *J. Am. Chem. Soc.* **1991,** *113*, 8419-8425.

(20) Popescu, D.-L.; Chanda, A.; Stadler, M.; de Oliveira, F. T.; Ryabov, A. D.; Münck, E.; Bominaar, E. L.; Collins, T. J., High-valent First-row transition-metal Complexes of Tetraamido (4N) and Diamidodialkoxido or Diamidophenolato (2N/2O) Ligands: Synthesis, Structure, and Magnetochemistry. *Coord. Chem. Rev.* **2008,** *252*, 2050-2071.

(21) Sharma, S. K.; Upreti, S.; Gupta, R., Effect of Ligand Architecture on the Structure and Properties of Square-Planar Nickel(II) Complexes of Amide-Based Macrocycles. *Eur. J. Inorg. Chem.* **2007,** *2007*, 3247-3259.

(22) Shinagawa, T.; Garcia-Esparza, A. T.; Takanabe, K., Insight on Tafel Slopes from a Microkinetic Analysis of Aqueous Electrocatalysis for Energy Conversion. *Sci. Rep.* **2015,** 13801-13821.

(23) (a) Anxolabéhère-Mallart, E.; Costentin, C.; Fournier, M.; Nowak, S.; Robert, M.; Savéant, J.-M., Boron-capped Tris (glyoximato) Cobalt Clathrochelate as a Precursor for the Electrodeposition of Nanoparticles Catalyzing H_2 Evolution in Water. *J. Am. Chem. Soc.* **2012,** *134*, 6104-6107; (b) Sconyers, D. J.; Blakemore, J. D., Distinguishing Between Homogeneous and Heterogeneous Hydrogen-evolution Catalysis with Molecular Cobalt Complexes. *Chem. Commun.* **2017,** *53*, 7286-7289; (c) Cobo, S.; Heidkamp, J.; Jacques, P. A.; Fize, J.; Fourmond, V.; Guetaz, L.; Jousselme, B.; Ivanova, V.; Dau, H.; Palacin, S.; Fontecave, M.; Artero, V., A Janus Cobalt-based Catalytic Material for Electro-splitting of Water. *Nat. Mater.* **2012,** *11*, 802-807.

(24) Kowalski, G.; Pielichowski, J.; Grzesik, M., Characteristics of Polyaniline Cobalt Supported Catalysts for Epoxidation Reactions. *Sci. World J.* **2014,** *2014*, 648949-648957.

TOC graphic

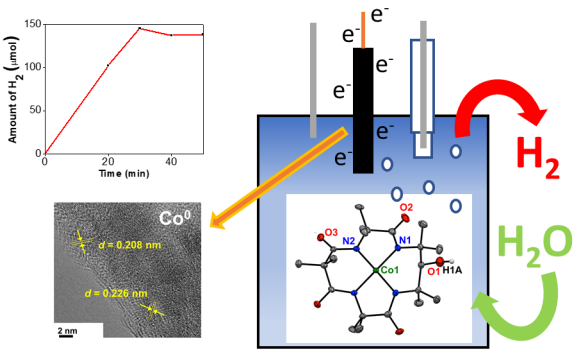
Amount of H2 (μmol)
150
100
50
0
0
20
40
Time (min)
Co0
d = 0.208 nm
d = 0.226 nm
2 nm
e-
e-
e-
e-
e-
e-
H2
H2O
O2
O3
N2
N1
Co1
O1
H1A